Low-Frequency Conducted Emissions Assessment for Electric Powertrain

Douglas Nascimento*
University of Zielona Góra
University of Twente
Hitachi Energy
eng.douglas.a@ieee.org

Lu Wan
AAU Energy
Aalborg University
Aalborg, Denmark
luwa@energy.aau.dk

Michał Przybylski
Institute of Automatic Control,
Electronics and Electrical Engineering
University of Zielona Góra
m.przybylski@iee.uz.zgora.pl

Flavia Grassi
Dipartimento di Elettronica,
Informazione e Bioingegneria
Politecnico di Milano
Milan, Italy
flavia.grassi@polimi.it

Robert Smolenski
Institute of Automatic Control,
Electronics and Electrical Engineering
University of Zielona Góra
Zielona Góra, Poland
r.smolenski@iee.uz.zgora.pl

Piotr Lezynski
Institute of Automatic Control,
Electronics and Electrical Engineering
University of Zielona Góra
Zielona Góra, Poland
p.lezynski@iee.uz.zgora.pl

Abstract—**The conducted emissions (CE) in powertrain applications are a major concern due to the high current peaks and transients from torque profiles and sudden speed changes. This paper investigates the time-domain noises analytically through a curve-fitting process, whose results can be used to reproduce the noise waveforms avoiding the need to store the entire waveform. Besides, common-mode (CM) and differential-mode (DM) voltages from speed changes of a PMSM (permanent magnet synchronous motor) powertrain are compared, in terms of harmonic components and noise amplitude, by using line impedance stabilization networks (LISN) from DO-160G and CISPR 25. It was observed that DM emissions, at low frequencies, are better coupled to DO-160G LISN and increase progressively with speed rise, while CM noise levels are kept constant.**

Index Terms—**Electromagnetic compatibility, PMSM, time-domain analysis, frequency-domain analysis.**

I. INTRODUCTION

The electric powertrains have progressively been embedded with sensors and electronics as a typical case of electromagnetic interference (EMI) coexistence in different frequency ranges. The powertrain emits either radiated or conducted emissions, which may cause malfunctions or unexpected shutdown of the embedded electronics and electric systems [1], [2]. Since these emissions affect the electromagnetic environment, various normative requirements are applied to systems infrastructure, addressing both stand-alone devices and entire fully equipped electric vehicles (EV). The issue behind this is that the frequency range of such regulations is higher than 150 kHz, i.e. not allowing to assess low frequency.

Concerning this frequency range restriction, this study investigates EMI analysis of low-frequency testbench using DO-160G normative, since the CISPR-25 standard, solely, jeopardizes the results for frequencies below 150 kHz due to harmonic filtering provided by the LISN topology [3]. The

applicability of the current study resides in investigating the 10-150 kHz frequency range in different operation conditions, comparing EMI levels with standards, and evaluating related EMC issues.

Therefore, the main contribution of this work relies on the evaluation of conducted emissions using an analytical model in the time domain (TD), whose results can be used to reproduce the noise waveforms. In addition, a possible application is provided through the EMI levels of the electric powertrain comprehending low-frequency range, below 150 kHz, by following DO-160G normative.

II. CONDUCTED EMISSIONS IN POWERTRAIN SYSTEMS

The conducted noise disturbances in powertrains are classified into common mode (CM) and differential mode (DM) emissions and are measured by voltage or current magnitude, as shown in Fig. 1. The CM current (red curve) flows from the inverter to the ground through parasitics components and causes CM voltage in neutral point, thus, enabling CM noise source. CM is worsened due to unbalanced three-phase circuit. The parasitic capacitances C_s and C_M from the heat sink and motor represent the highest capacitances in the CM path [4]. On the other hand, the DM current (blue curve) flows in phase conductors at the same time, and it is inherent to the circuit characteristics [5]–[7].
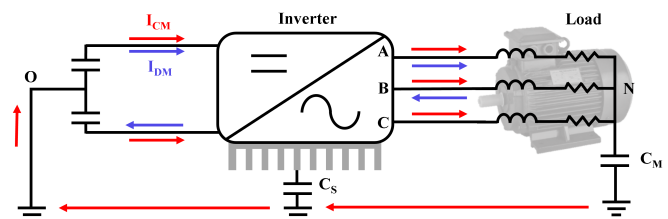

Fig. 1: Currents CM (I_{CM}) and DM (I_{DM}) in a powertrain.

The CM disturbance mainly causes the high-frequency emissions (from the switching frequencies up to tens of MHz),

due to the transient CM noise (dv/dt and di/dt) flowing the CM path. This type of noise can be mitigated by using CM chokes. The DM noise is associated with low-frequency emissions and is mostly due to the PWM switching pattern [6], which is often suppressed by the capacitor at the dc-link voltage bus [8].

The CM noise emission is considered the most disturbing and cumbersome to troubleshoot within conducted emission range of frequency [8] and can be mitigated by using EMI filters (chokes) or different PWM techniques such as space vector PWM, active zero state PWM, and near state PWM. However, the theoretical zero CM voltage cannot be achieved due to the odd number of legs from two-level inverters [6].

The harmonic analysis for phase voltages can be expressed in terms of summing of arithmetic sequences [9] as,

$$U_{am,n}(t) + U_{bm,n}(t) + U_{am,n}(t) =$$
$$\frac{4V_{DC}}{\pi}\frac{1}{m}J_n\left(m\frac{\pi}{2}M\right)\sin\left([M+n]\frac{\pi}{2}\right)[1 + 2\cos n\frac{2\pi}{3}]cos$$
$$\times\left(m\omega_c t + n(\omega_0 t)\right) \quad (1)$$

Thus, the CM components can be obtained by using double Fourier series analysis on the signal expressed by [9],

$$u_{CM}i(t) = \frac{4V_{DC}}{3\pi}\sum_{m=1}^{\infty}\sum_{\substack{n=-\infty,\\n\neq 0}}^{\infty}\frac{1}{m}J_n\left(m\frac{\pi}{2}M\right)$$
$$\times\sin\left([m+n]\frac{\pi}{2}\right)\left[1+2\cos n\frac{2\pi}{3}\right]\cos(m\omega_c t + \omega_0 t) \quad (2)$$

and the DM component can be obtained as,

$$u_{DM}i(t) = \frac{8V_{DC}}{\sqrt{3}\pi}\sum_{m=1}^{\infty}\sum_{n-\infty}^{\infty}\frac{1}{m}J_n\left(m\frac{\pi}{2}M\right)$$
$$\times\sin\left([m+n]\frac{\pi}{2}\right)\sin\left(\frac{n\pi}{3}\right)\cos(m\omega_c t + \omega_0 t) \quad (3)$$

For the even combinations of $m \pm n$, the side-band harmonics will not appear in the harmonic sum, due to the term $([m + n]\pi/2)$, i.e., the spectrum shows only odd harmonic components. In the case of elimination of term $[1 + 2\cos[(n2\pi/3)]$, there is a cancellation on the harmonics in CM voltage, nevertheless, appearing in DM voltage due to the term $\sin(n\pi/3)$.

The analysis of harmonics in the current study is obtained by converting the time-domain voltage waveforms measured at DC LISN into the frequency domain by using FFT. Thus, the values for common-mode voltages (V_{CM}) can be obtained by $V_{CM} = (V1 + V2)/2$, while for DM (V_{DM}) is obtained through $V_{DM} = (V1 - V2)$ [10].

III. Time-Domain Decomposition of Ringing Effect

The objective of proposing a time-domain analysis of noise waveforms is to provide an analytical approach to reproduce the noise waveform. Instead of storing the entire waveform, the analytical process only requires the storage of a small set of parameters that may describe the statistical properties of the entire waveform.

The time-domain waveforms of CE noise show a periodical pattern when the powertrain is running steadily at a constant speed. This periodic pattern is made up of ringing signals, caused by the turn-on and turn-off of the power switches, which induces the high dv/dt and di/dt. This typical ringing noise can be analytically expressed as [11]:

$$y(t) = Ae^{-\pi\frac{f}{Q}(t-t_1)}\sin\left(2\pi f\left(t - t_1\right)\right) \quad (4)$$

where A is the amplitude, Q is the damping factor, f is the frequency of a sinusoidal wave, and t_1 is a time shift.

After analyzing their ringing pattern, this study will decompose the time-domain noise waveforms into several ringing signals. The curve-fitting technique is applied to each ringing signal by optimization algorithm to obtain the four parameters in (4). This work uses the pattern search algorithm rather than the conventional least-square error method. Although the pattern search method may be computationally expensive, it is more versatile and can handle complex models than the least-square error method.

IV. Methodology

The measurements were carried out in a testbench, seen in Fig. 2, composed of a commercial off-the-shelf two-wheel electric powertrain with permanent magnet synchronous motor (PMSM), 1500 W, 3200 RPM, powered by a gearbox, a speed and direction user controller. The speed under analysis was displayed in real-time in the dashboard, controlled by a power switch control box (inverter and PWM controller) supplied by 48 V DC power supply connected to DC LISN compliant with either CISPR-25 standard or DO-160G test procedures - under different topology configurations set by the user.
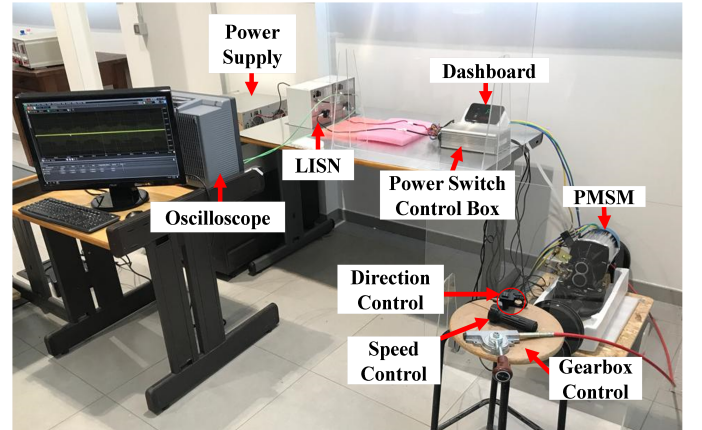

Fig. 2: Setup used for emissions assessment of the powertrain.

Those standards were chosen to provide investigations in the low-frequency range due to their applicability. Since the CISPR-25 frequency range is 150 kHz – 960 MHz, the tests also included the standard DO-160G (ranging from 10 kHz to 400 MHz).

The measurement tests were carried out by using an oscilloscope on 250 MS/s resolution, increasing the speed in

TABLE I: Specification of the devices used in the test.

Device	Specification
Power Supply	Eutron Rivoli-Italia BVR 2000 150-12
DC LISN	High Voltage Artificial Network TESEQ Mod. HV-AN 150
Power Switch Control Box	Generic SPWM, 3200 RPM, 1500 W of Rated Output Power
Motor	Permanent Magnet Synchronous Motor (PMSM)
Oscilloscope	Keysight MXR604A, 6 GHz 10 Gsa/s 10 bit, infiniium MXR-Series
Powertrain	Electric two-wheel integrated rear axle, brake universal group, Mod. N. 60

10km/h steps from 10 - 40 km/h, with the current peak varying from 1.57 A to 6.10 A. The specification of the devices used is found in Table I. By comparing the spectrum obtained from different setups, it turns out to be possible to assess the impact of using those standards (intended for different applications) on measurements of the powertrain's conducted emissions. The measurement was obtained with time-domain analysis due to the convenience of both possibilities to convert to frequency-domain (FD) using Discrete Fourier Transform (by Fast Fourier Transform algorithm) and to register torque load profile and speed changes, allowing to track transient states.

V. LOW FREQUENCY ASSESSMENT FROM CE

In this section, the modeling results of noise waveforms are shown in Section V-A. Then, EMI spectrum comparison charts from CISPR-25 and DO-160G are discussed in Section V-B. Finally, the EMI peak levels within different speed changes are shown in Section V-C.

A. Modeling Results of Noise Waveforms

One example of phase voltage measured at the LISN is shown in Fig. 3, where the envelope of the noise peaks exhibits a sinusoidal pattern. Therefore, the noise waveforms can be reproduced easily once one period signal can be described analytically.
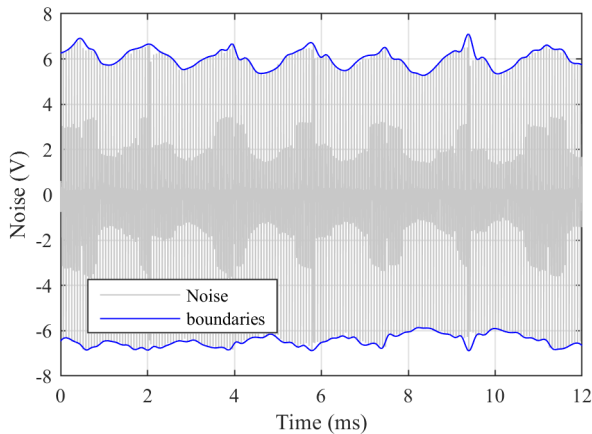
Fig. 3: Measured noise signal of one phase voltage at LISN DO-160G.

To this end, the noise waveform in Fig. 3 is zoomed into two repeated periods, as shown in Fig. 4, where two kinds of ringing signals are present in each period. One of them

has a smaller amplitude (in the red region, hereinafter called undershoot ringing noise), and another has a bigger amplitude (blue region, hereinafter called overshoot region), whose peaks form the envelope of the noise waveform.
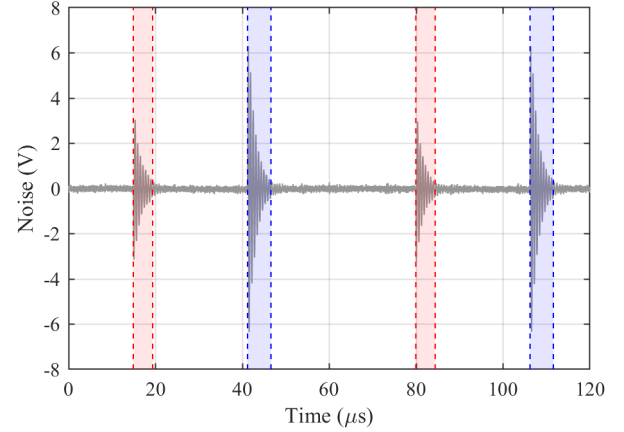
Fig. 4: A portion of noise in Fig. 3 with two types of ringing signals highlighted: smaller amplitude (red regions) and larger amplitude (blue regions).

To fit the two types of ringing signals in Fig. 4, a pattern search strategy is implemented in the MATLAB routine for optimizing the four parameters in (4). The fitted waveforms of two ringing signals are compared with the original noises in Fig. 5 and Fig. 6, respectively.
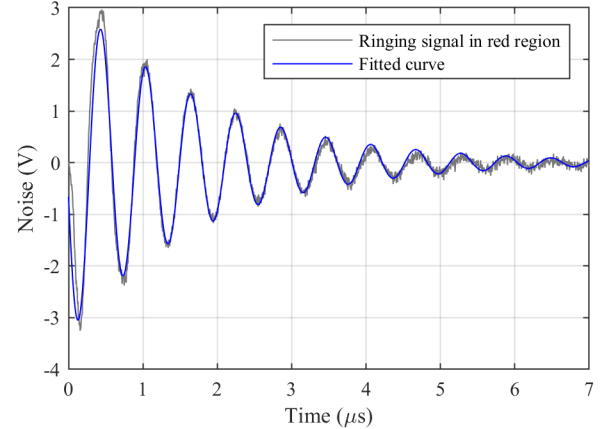
Fig. 5: Fitted curve vs the smaller ringing signal in red region of Fig. 4.

Table II summarizes the optimized four parameters in (4) of the ringing signals. It shows that the fitted waveform can represent the original waveforms in most of the noise. The large discrepancies occur at the beginning of the ringing waveform, where the noise has a larger steep slope. The level of fitness can be expressed in terms of normalized mean square error (NMSE). For the undershoot and overshoot fitted curves, the NMSE are 0.0604 and 0.1131, respectively.

A possible application for the noise and waveform analysis is the DM and CM from a mini electric powertrain considering different standards applications.
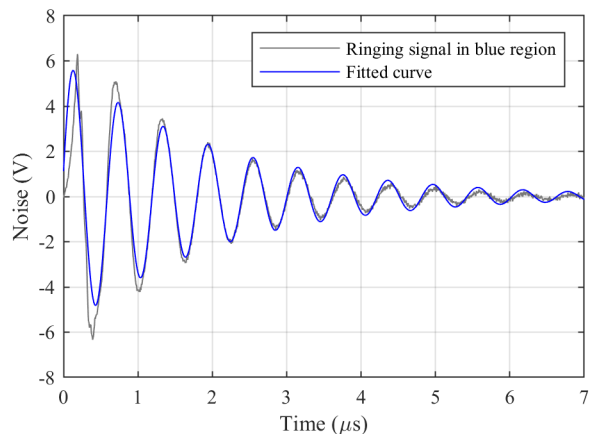
Fig. 6: Fitted curve vs the bigger ringing signal in blue region of 4.

TABLE II: Fitted parameters for ringing signals.

Waveforms	Parameters			
	$A(V)$	Q	$f(MHz)$	$t_1(\mu s)$
Undershoot ringing	- 3.31	9.48	1.65	- 0.0196
Overshoot ringing	6.00	10.72	1.65	- 0.0183

B. Comparing EMI Levels between CISPR-25 and DO-160G

The frequency spectra of CM and DM voltages according to CISPR-25 and DO-160G are seen in Fig. 7, with modulation frequency as 310 Hz (for 10 km/h) and switching frequency of 15.380 kHz. This figure shows that low-frequency DM (at 310 Hz) is coupled with a higher EMI level for DO-160, though with a penalty of attenuation of CM around 50 kHz – which is, conversely, better observed when using CISPR-25. These variations can be attributed to the LISN topology used, mainly due to components' resonances being triggered. In addition, the CM noise voltage exhibits an EMI peak, caused by parasitic CM path, at 1.6 MHz, which reaches 100 dBuV and it is coupled by both standards LISNs.

Since the frequency range covered by CISPR-25 is above 150 kHz, it is inappropriate to be used in these testbench measurements, due to the frequency range of interest being below its bandwidth.

C. Conducted Emissions in Different Speed Conditions

The speed-changing profiles and EMI emission levels are seen in Fig. 8, focusing on DM EMI levels (since CM path does not change). The DM voltage shows different components below 2 kHz, caused by the motor operation at different speeds: (a) at 310 Hz for 10 km/h, reaching 83 dBuV; (b) at 560 Hz for 20 km/h, with EMI level at 93 dBuV, (c) at 830 Hz for 30 km/h, on 98 dBuV and; (d) at 1080 Hz for 40 km/h, with 104 dBuV. These variations in the emissions can be attributed to the rise of the internal motor voltage, due to the increase of modulation frequency to run the motor at higher speed. It is highlighted that the torque remains always the same since the motor was operating at no load condition. However, it has the intrinsic torque to beat the inertia and it is
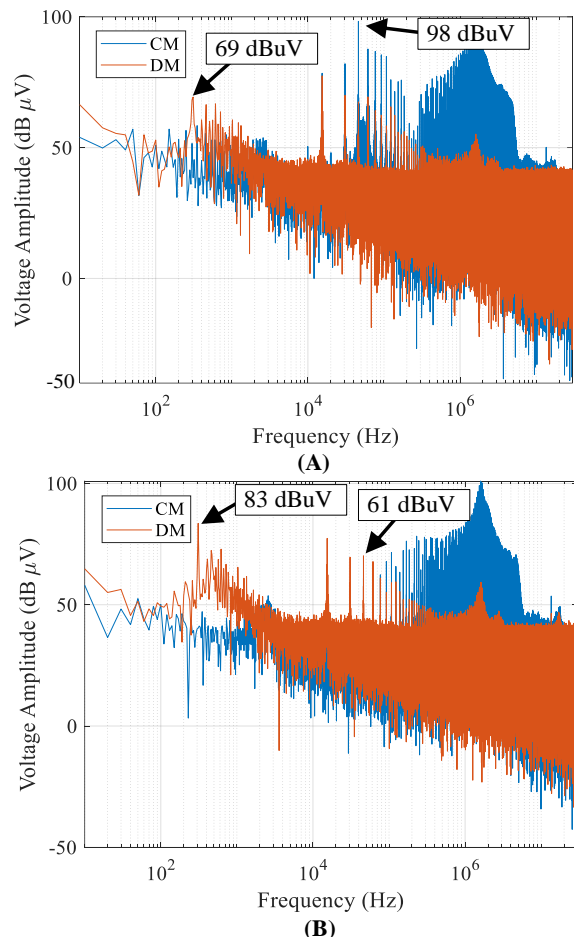

Fig. 7: Comparison of spectrum for testbench running at $10\,\mathrm{km/h}$: (A) CISPR-25 and (B) DO-160G.

probably the reason behind the increasing emission into $10\,\mathrm{dB}$ from 10 km/h to 20 km/h.

As a summary, the EMI levels chart from the speed profile basically demonstrates three things: (a) The fundamental and highest harmonic component is tied to the frequency used to control the speed of the motor (modulation frequency). (b) CM voltage does not change with the speed as expected - since there is no change in the CM path. (c) The highest EMI peak level comes from the greatest speed due to the increase of modulating frequency, as shown in a previous study [12].

VI. CONCLUSION

The equation of a damping sinusoidal waveform is used to fit two ringing signals in the noise waveform by applying a pattern search algorithm, through time-domain analysis. The fitted equations can be used to reproduce the time-domain waveforms of the noise measured in the powertrain testbench.

As an application for the waveform analysis, the CM and DM voltage noises from an electric powertrain were analyzed in the frequency domain. The voltage sources were obtained from speed changes in the time domain to allow low-frequency emissions harmonic components and amplitude assessment.

Thereby, the TD and FD analysis on electric powertrain signals provides a better understanding of switching transients
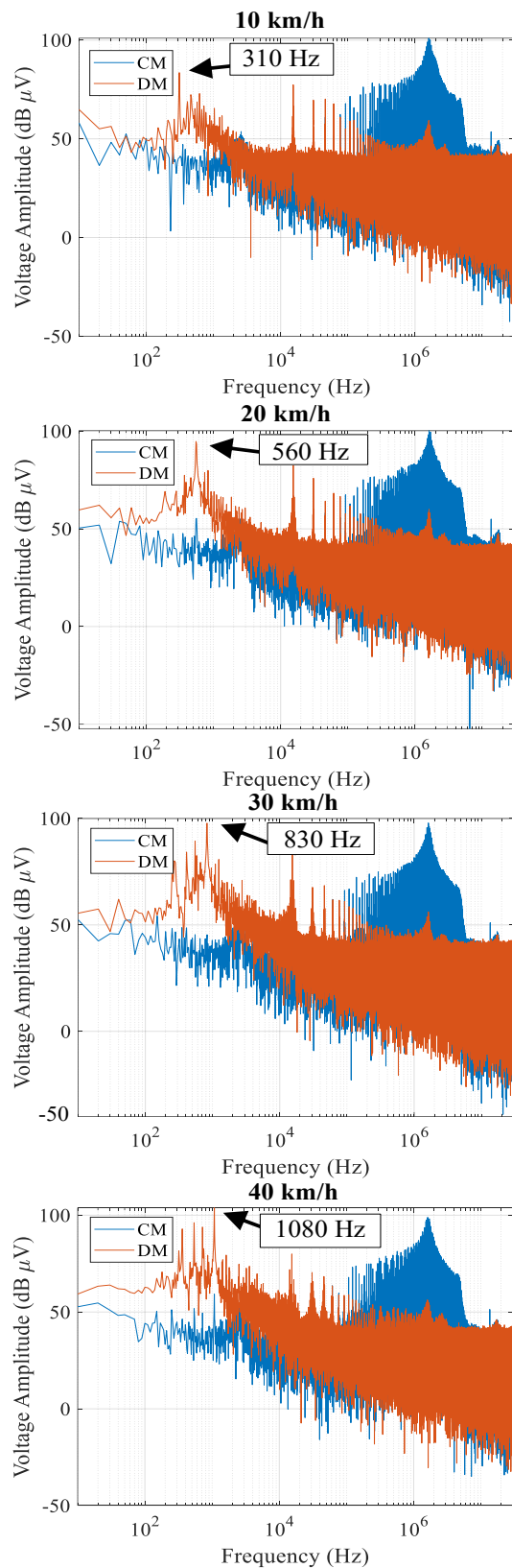
Fig. 8: EMI levels by DO-160G setup at (charts from top to bottom): 10 km/h, 20 km/h, 30 km/h and 40 km/h.

and EMI levels for their subsequent mitigation of ringing effects and improve the EMC for EV applications.

REFERENCES

[1] L. Wan, A. Hamid, F. Grassi, G. Spadacini, and S. A. Pignari, "Spice simulation of modal impedances in automotive powertrains under different operating conditions," pp. 1–5, 2020.

[2] D. A. Nascimento, Y. Iano, H. J. Loschi, N. Razmjooy, R. Sroufe, V. D. J. S. Oliveira, D. A. P. Castro, and M. Montagner, "Sustainable adoption of connected vehicles in the brazilian landscape: Policies, technical specifications and challenges," *Transactions on Environment and Electrical Engineering*, vol. 3, p. 44, 2019.

[3] L. Wan, A. Khilnani, A. Hamid, F. Grassi, G. Spadacini, S. Pignari, M. Sumner, and D. Thomas, "Limitations in applying the existing lisn topologies for low frequency conducted emission measurements and possible solution," *Proceedings of the 2021 Asia-Pacific International Symposium on Electromagnetic Compatibility, APEMC 2021*, pp. 2021–2024, 2021.

[4] A. Kempski, R. Smolenski, and R. Strzelecki, "Common mode current paths and their modeling in pwm inverter-fed drives," *PESC Record - IEEE Annual Power Electronics Specialists Conference*, vol. 3, pp. 1551–1556, 2002.

[5] Y. Huang, J. Walden, A. Foote, H. Bai, D. Lu, F. Jin, and B. Cheng, "Analytical characterization of cm and dm performance of three-phase voltage-source inverters under various pwm patterns," *IEEE Transactions on Power Electronics*, vol. 36, pp. 4091–4104, 2021.

[6] D. Jiang, J. Chen, and Z. Shen, "Common mode emi reduction through pwm methods for three-phase motor controller," *CES Transactions on Electrical Machines and Systems*, vol. 3, pp. 133–142, 2019.

[7] J. Hu, X. Xu, D. Cao, and G. Liu, "Analysis and optimization of electromagnetic compatibility for electric vehicles," *IEEE Electromagnetic Compatibility Magazine*, vol. 8, pp. 50–55, 2019.

[8] B. Revol, J. Roudet, J. L. Schanen, and P. Loizelet, "Emi study of three-phase inverter-fed motor drives," *IEEE Transactions on Industry Applications*, vol. 47, pp. 223–231, 2011.

[9] A. Kempski, "Decomposition of emi noise into common and differential modes in pwm inverter drive system," *Electrical Power Quality and Utilisation Journal*, vol. XII, pp. 53–58, 2006.

[10] K. S. Kostov, S. Schroth, F. Krismer, M. Priecinsky, H. P. Nee, and J. W. Kolar, "The input impedance of common-mode and differential-mode noise separators," *IEEE Transactions on Industry Applications*, vol. 51, pp. 2352–2360, 5 2015.

[11] X. Liu, F. Grassi, F. Trotti, and W. Hirschi, "Behavioral modeling of an off-the-shelf damped sinusoidal transient generator," *IEEE Letters on Electromagnetic Compatibility Practice and Applications*, vol. 4, pp. 56–60, 4 2022.

[12] D. Nascimento, R. Smolenski, P. Lezynski, A. Matthee, N. Moonen, and F. Leferink, "Versatile lab view-fpga-based testbench for electromagnetic interference evaluation in vsds," *IEEE International Symposium on Electromagnetic Compatibility*, vol. 2022-Septe, pp. 764–769, 2022.